

Characterization and reduction of unexplained noise in superconducting transition-edge sensors

J. N. Ullom,^{a)} W. B. Doriese, G. C. Hilton, J. A. Beall, S. Deiker, W. D. Duncan, L. Ferreira, K. D. Irwin, C. D. Reintsema, and L. R. Vale
National Institute of Standards and Technology (NIST), 325 Broadway, Boulder, Colorado 80305

(Received 28 January 2004; accepted 24 March 2004; published online 7 May 2004)

The noise in superconducting transition-edge sensors (TESs) commonly exceeds simple theoretical predictions. The reason for this discrepancy is presently unexplained. We have measured the amplitude and frequency dependence of the noise in TES sensors with eight different geometries. In addition, we have measured the dependence of the noise on operating resistance, perpendicular magnetic field, and bath temperature. We find that the unexplained noise contribution is inversely correlated with the temperature width of the superconducting-to-normal transition and is reduced by a perpendicular field and in certain geometries. These results suggest paths to improved sensor performance. © 2004 American Institute of Physics. [DOI: 10.1063/1.1753058]

Transition-edge sensors (TESs) are a promising technology for precision measurements of electromagnetic radiation at γ -ray, x-ray, optical, and far-infrared to millimeter wavelengths.^{1–4} These sensors consist of superconducting thin films electrically biased in the resistive transition. TESs are likely to be used in several large upcoming measurement programs, including studies of polarization in the cosmic microwave background, next-generation ESA and NASA x-ray satellites, and the sub-millimeter array SCUBA 2. The ability of TESs to perform broadband, high-efficiency, and high-resolution x-ray spectroscopy also makes them powerful tools for terrestrial materials analysis.⁵ The best energy resolutions obtained with TESs (~ 2 eV full width at half maximum (FWHM) at 1.5 keV and 4 eV at 5.9 keV) are roughly 30 times better than for ubiquitous silicon–lithium sensors. This performance level allows technologically relevant nanometer-scale particles and films to be analyzed by use of closely spaced low-energy x-ray lines.

The resolution of TESs is approaching but has not yet reached the predicted theoretical limits. Given the large range of applications, there is considerable interest in either improving sensor performance or better defining the performance limits. The known sources of noise in TES sensors are Johnson noise and thermodynamic fluctuations in the device thermal conductances. One factor that contributes to the discrepancy between experiment and theory is the presence of noise that is not explained by these two mechanisms. This unexplained noise (UN) has been observed by numerous groups using TESs made in very different ways. While not all observations are identical, many groups observe UN that exceeds the Johnson noise at high frequencies and that falls below the contribution of thermodynamic fluctuations in the connection to the heat bath (so-called phonon noise) at frequencies less than the thermal-response knee.^{6,7} It has previously been observed that weak links reduce the UN.^{8–12} It has also been observed that perpendicular magnetic fields reduce the UN.¹⁰ Despite these observations, significant work remains to be done in characterizing the UN, in par-

ticular, in quantifying how its magnitude depends on TES geometry and operating characteristics. A better description of the UN will enable better sensor designs and help guide efforts to find an explanation. Possible causes of the UN include internal thermal fluctuations¹³ and fluctuational superconductivity.^{7,14} While both mechanisms have been used to explain the behavior of specific sensor designs, a universal theory is lacking.

In this letter, we present measurements of the UN in TES devices with eight different geometries, many of which have not been previously studied. We also present measurements of the UN in one TES geometry as a function of perpendicular magnetic field, bias point, and bath temperature. Most strikingly, we observe a strong inverse correlation between the magnitude of the UN and the temperature width of the superconducting-to-normal transition. We present an empirical expression for the magnitude of the UN that appears valid over a broad, but not universal, range of conditions, and discuss the impact of the UN on the energy resolution of a calorimeter.

The TES devices in this study consisted of bilayers of Mo and Cu with transition temperatures near 100 mK. The devices were fabricated using our standard process, which includes an additional Cu layer for edge passivation.¹⁵ The devices are shown in Figs. 1(a)–1(h). Figure 1(a) is the standard sensor. We have previously achieved x-ray resolutions of 4.5 eV FWHM at 5.9 keV in devices with this geometry.² The devices in Figs. 1(b)–1(g) have additional Cu normal metal features deposited on the bilayer in the same step as the edge passivation. These features suppress superconductivity in the underlying bilayer and take the form of bars or islands. The device in Fig. 1(h) has only edge passivation but is shaped like a wedge.

Measurements were conducted at bath temperatures below 100 mK. Each sensor was voltage biased by a smaller shunt resistor R_{sh} , and the sensor current was measured by a superconducting quantum interference device (SQUID) amplifier. Traditionally, the difficulty of implementing multiple amplifier chains has limited the number of sensors that can be characterized. We have overcome this difficulty by using

^{a)}Electronic mail: ullom@boulder.nist.gov

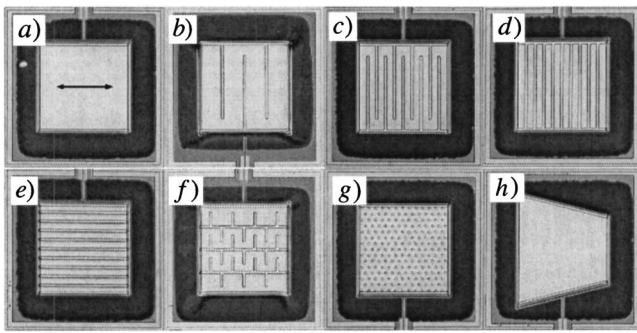


FIG. 1. Micrographs of TES sensors on Si_3N_4 membranes. The arrow in (a) indicates the direction of bias current in all devices. Cu passivation is present on TES edges parallel to the bias current. Square sensors are $400\ \mu\text{m}$ on a side: (a) standard pixel with $R_N=14\ \text{m}\Omega$; (b) sparse normal bars partially span the device perpendicular to the bias current; (c) dense partial perpendicular bars; (d) dense full perpendicular bars; (e) dense parallel bars; (f) parallel and perpendicular bars; (g) islands; (h) wedge. Cu bars are $10\ \mu\text{m}$ wide and $500\ \text{nm}$ thick. Cu islands are $5\ \mu\text{m}$ in diameter and $500\ \text{nm}$ thick.

a SQUID multiplexer system¹⁶ that allowed all the devices to be measured in a single cryostat cycle. The sensors were mounted in a light-tight enclosure and shielded from magnetic fields by mu-metal and superconducting tape. A calibrated field coil was positioned inside the magnetic shielding. The magnitude of the residual field was determined from the coil field that maximized the transition temperature T_c of the sensors, and thereafter the coil was used to control the field component B perpendicular to the sensors. Small apertures in the sample enclosure were masked by foil to reflect infrared radiation but transmit x rays from a Fe-55 source on the 4.2 K stage. A cold shutter allowed the sensors to be studied with and without x rays.

Sensor properties were obtained in the following manner. The normal state resistance R_N , operating resistance R , bias current I , and bias power P_b were obtained from current–voltage curves. The thermal conductance of the membrane G_o was obtained from current–voltage curves taken at a range of bath temperatures T_b . Pulse records from x rays were recorded with a digitizer. The intrinsic time constant τ_o was obtained from pulse decay times with $T_b \approx T_c$. The heat capacity C obtained from $G_o\tau_o$ agreed closely with a theoretical estimate based on an average of the normal and fully superconducting values. The spectral density of the output current noise I_N was measured with a spectrum analyzer. The parameter $\alpha=(T/R)(dR/dT)$, a dimensionless measure of the transition width, is sufficiently important that two extraction methods were used. The primary method was to deduce α from the measured fall time τ of an x-ray pulse using the relation $\alpha_\tau=[(\tau_o/\tau)-1](G_oT_c/P_b)(1+\eta)/(1-\eta)$ where $\eta=R_{sh}/R$. This method provides a reliable way of obtaining relative values of α for the different geometries. However, some quantitative error in α_τ was expected since the pulse decays were not perfectly exponential. Consequently, we also used G_o to calculate the internal device temperature and then α_{I-V} at each point on the current–voltage curves. For $\alpha_{I-V}<200$, there was a near-perfect linear correlation between α_{I-V} and α_τ . For higher values of α_{I-V} , the current–voltage method becomes unreliable since P_b and the device temperature change very little in the transition. The values α_{I-V} yielded excellent fits to I_N in cases

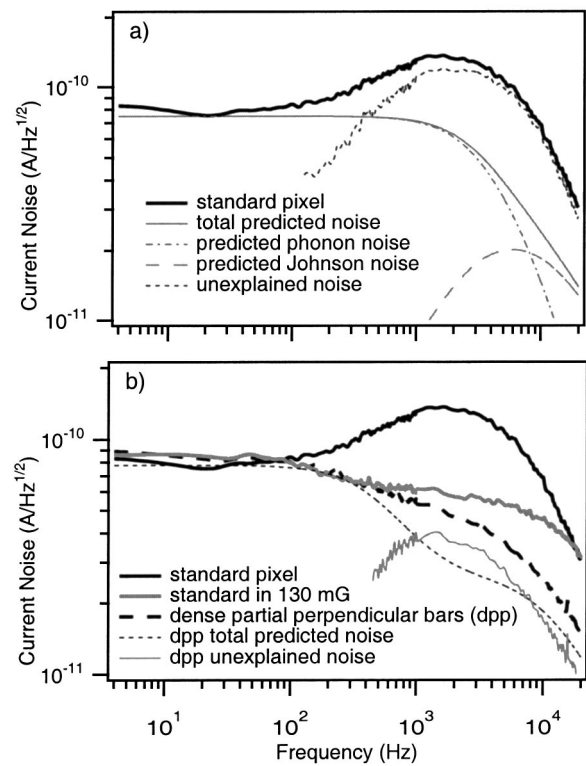


FIG. 2. (a) Measured spectral density of output current in standard pixel at $60\% R_N$ and $B=0$. Predicted noise contributions and the difference between data and theory are also shown. This difference is the unexplained noise; (b) measured spectral density from the standard pixel at $60\% R_N$ and $B=0$, the standard pixel at $60\% R_N$ and $B=130\ \text{mG}$, and the dense partial perpendicular bar pixel [Fig. 1(c)] at $60\% R_N$ and $B=0$. Significant UN suppression can be observed. Predicted and unexplained noise contributions are shown for the dense partial perpendicular pixel.

where the loop gain was low and I_N depends strongly on α . Since the values α_{I-V} were consistently 70% larger than the values α_τ in the $\alpha_{I-V}<200$ regime, the α values used in this letter are given by $1.7\alpha_\tau$.

Figure 2(a) shows the measured I_N for the standard pixel of Fig. 1(a). The magnetic field is tuned to zero, $T_b=89.3\ \text{mK}$, and the sensor is biased at $R/R_N=60\%$. Also shown are the total predicted noise, the predicted phonon noise, the predicted Johnson noise, and the quadrature difference between the measured and predicted noise. The predictions were generated using standard expressions.¹⁷ The measured and predicted noise agree at low frequencies, but an unexplained noise source is present at higher frequencies. The rolloff near $10\ \text{kHz}$ is due to the self-inductance of the measurement circuit. The UN is reduced by geometry and field as shown in Fig. 2(b) where I_N is plotted for the standard pixel, a device with densely spaced partial perpendicular bars [Fig. 1(c)], and the standard pixel in a field of $130\ \text{mG}$. Also shown are the predicted noise and the UN for the bar device. The UN is much smaller than in Fig. 2(a) and is about twice the Johnson noise. In the remainder of this letter, the magnitude M of the UN in a device will be given by its peak value (in $\text{A}/\sqrt{\text{Hz}}$) divided by the zero-inductance high-frequency limit of the Johnson noise.

The parameter space for the UN is large: for each device, it spans T_b (and hence P_b), R , and B . A partial mapping of the UN over this space is shown in Fig. 3. The magnitude of the UN is plotted versus α for $T_b=89.3\ \text{mK}$, $R/R_N=60\%$,

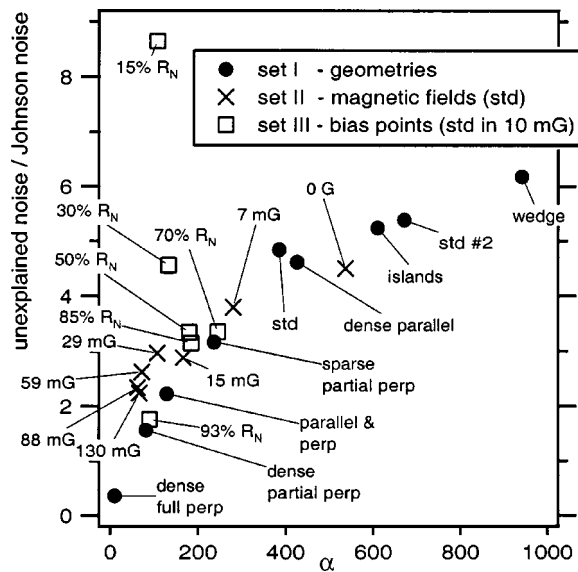


FIG. 3. Ratio of unexplained noise to Johnson noise vs α for three data sets: Set I (filled circles) different geometries at constant bias point and magnetic field; set II (crosses) standard geometry at constant bias point but different magnetic fields; set III (squares) standard geometry at different bias points and constant magnetic field. A point for 7% R_N with a noise ratio of 13.3 and $\alpha=85$ has been omitted.

and $B=0$ for nine devices: the eight devices of Fig. 1, and a duplicate of the standard pixel (set I—circles). The magnitude of the UN is also plotted versus α for the standard pixel at $T_b=89.3$ mK, $R/R_N=60\%$, and $B=0-130$ mG (set II—crosses). Finally, the UN is shown for the standard pixel at $B=10$ mG, $T_b=89.3$ mK, and $R/R_N=7-93\%$ (set III—squares). It can be seen from the points in set I that M is strongly correlated with α and that it is reduced below unity for $\alpha<25-30$. The points in set I can be approximately fit by the expression $M=0.2\sqrt{\alpha}$, and the absence of outliers suggests that the details of device geometry are important only insofar as they affect α .

It can be seen from the points in set II that magnetic field simultaneously reduces the UN and α . The points in set II lie slightly above the points in set I, suggesting that device geometry may be a more effective means of reducing the UN while preserving α . The difference between the 0 G point in set II and the standard (std) point in set I is attributed to imperfect field nulling.

Set III in Fig. 3 (squares) shows the dependence of UN and α on R/R_N . For $R/R_N \geq 50\%$, the points in set III lie on the curve defined by set I. For $R/R_N < 50\%$, there is more UN present for a given value of α than in set I. This increase indicates that the UN depends on other parameters in addition to α , and that the UN is enhanced at low R/R_N .

Not shown in Fig. 3 are a series of measurements taken with the standard device at $R/R_N=60\%$, $B=10$ mG, and $T_b=57-98$ mK. The bias power changes over this range of T_b by a factor of 17. All the points fall on the curve of set I, suggesting that the dependence of the UN on voltage and current density is weak. We have also studied the different geometries of set I at resistance fractions above and below 60%. Geometries that reduce the UN at 60% R_N also reduce the UN at other resistance fractions.

The effects of the UN on calorimeter performance can be estimated using these measurements and expressions in Ref. 18. For example, the small-signal energy resolution of the standard pixel in set I is calculated to be 1.0 eV FWHM from the theoretical noise, but 1.9 eV when the UN is included. For comparison, UN is calculated to degrade the FWHM resolution of the dense partial perpendicular bar device from 2.2 to 2.9 eV. The reduction of UN in certain geometries and fields suggests a route to improved performance: a design with low C and low α . In a perpendicular bar device with $\alpha=30$ and C reduced to yield the same saturation energy and response time as the standard pixel, the predicted resolution in the presence of UN is below 1.3 eV.

In summary, we have measured the UN in a range of TES geometries and operating points. The UN is strongly correlated with α , and it can be suppressed using both device geometry and an applied field. Future work will focus on a microscopic explanation for the UN and a detailed optimization of calorimeter design.

This work was supported in part by NASA under Grant No. NDPR S06561-G.

- ¹M. F. Cunningham, J. N. Ullom, T. Miyazaki, S. E. Labov, J. Clarke, T. M. Lanting, A. T. Lee, P. L. Richards, J. Yoon, and H. Spieler, *Appl. Phys. Lett.* **81**, 159 (2002).
- ²K. D. Irwin, G. C. Hilton, J. M. Martinis, S. Deiker, N. Bergren, S. W. Nam, D. A. Rudman, and D. A. Wollman, *Nucl. Instrum. Methods Phys. Res. A* **444**, 184 (2000).
- ³B. Cabrera, R. M. Clarke, P. Colling, A. J. Miller, S. Nam, and R. W. Romani, *Appl. Phys. Lett.* **73**, 735 (1998).
- ⁴J. M. Gildemeister, A. T. Lee, and P. L. Richards, *Appl. Phys. Lett.* **74**, 868 (1999).
- ⁵D. A. Wollman, K. D. Irwin, G. C. Hilton, L. L. Dulcie, D. E. Newbury, and J. M. Martinis, *J. Microsc.* **188**, 196 (1997).
- ⁶M. A. Lindeman, R. P. Brekosky, E. Feliciano, F. Finkbeiner, M. Li, C. K. Stahle, C. M. Stahle, and N. Tralshawala, in *Low Temperature Detectors*, edited by F. S. Porter, D. McCammon, M. Galeazzi, and C. K. Stahle, AIP Conference Proceedings vol. 605 (AIP, Melville, NY, 2002).
- ⁷A. Luukanen, K. M. Kinnunen, A. K. Nuottajarvi, H. F. C. Hoevers, W. M. Bergmann Tiest, and J. P. Pekola, *Phys. Rev. Lett.* **90**, 238306 (2003).
- ⁸G. C. Hilton, K. D. Irwin, J. M. Martinis, and D. Wollman, U.S. Patent No. 6,239,431 (24 November, 1998).
- ⁹W. Bergmann Tiest, M. Bruijn, E. Krouwer, W. Mels, M. Ridder, and H. Hoevers, TES Workshop, Boulder, CO, April 2002.
- ¹⁰J. N. Ullom, W. B. Doriese, G. C. Hilton, J. A. Beall, S. Deiker, K. D. Irwin, C. D. Reintsema, L. R. Vale, and Y. Xu, *Nucl. Instrum. Methods Phys. Res. A* (in press).
- ¹¹J. G. Staguhn, S. H. Moseley, D. J. Benford, C. Allen, J. A. Chervenak, T. Stevenson, and W. Hsieh, *Nucl. Instrum. Methods Phys. Res. A* (in press).
- ¹²M. A. Lindemann, S. Bandler, R. P. Brekosky, J. A. Chervenak, E. Figueroa-Feliciano, F. M. Finkbeiner, T. Saab, and C. K. Stahle, *Nucl. Instrum. Methods Phys. Res. A* (in press).
- ¹³H. F. C. Hoevers, A. C. Bento, M. P. Bruijn, L. Gottardi, M. A. N. Korevaar, W. A. Mels, and P. A. J. de Korte, *Appl. Phys. Lett.* **77**, 4422 (2000).
- ¹⁴G. M. Seidel and I. S. Beloborodov, *Nucl. Instrum. Methods Phys. Res. A* (in press).
- ¹⁵G. C. Hilton, J. M. Martinis, K. D. Irwin, N. F. Bergren, D. A. Wollman, M. E. Huber, S. Deiker, and S. W. Nam, *IEEE Trans. Appl. Supercond.* **11**, 739 (2001).
- ¹⁶C. D. Reintsema, J. Beyer, S. W. Nam, S. Deiker, G. C. Hilton, K. D. Irwin, J. M. Martinis, J. N. Ullom, L. R. Vale, and M. MacIntosh, *Rev. Sci. Instrum.* **74**, 4500 (2003).
- ¹⁷See, for instance, J. M. Gildemeister, Ph.D. thesis, University of California, Berkeley, 2000 or Ref. 13.
- ¹⁸S. H. Moseley, J. C. Mather, and D. McCammon, *J. Appl. Phys.* **56**, 1257 (1984).